NJC

PAPER

View Article Online
View Journal | View Issue



Cite this: *New J. Chem.*, 2021, 45, 12108

# An experimental and theoretical exploration of supramolecular interactions and photoresponse properties of two Ni(II) complexes†

Samit Pramanik,[a] Sudipta Pathak,[b] Sumanta Jana,[a] Monotosh Mondal,[b] Antonio Frontera *[c] and Subrata Mukhopadhyay*[a]

Received 20th March 2021,
Accepted 2nd June 2021

DOI: 10.1039/d1nj01363g

rsc.li/njc

Two new nickel(II) complexes, $C_{32}H_2N_8NiClO_9$ (**1**) and $C_{36}H_{28}N_{12}NiOF_{24}P_4$ (**2**), have been synthesized where both 2,4,6-tri(pyridin-2-yl)-1,3,5-*s*-triazine and dipicolinic acid act as tridentate ligands for complex **1** and only 2,4,6-tri(pyridin-2-yl)-1,3,5-*s*-triazine is employed as a tridentate ligand for complex **2**. These complexes were characterized by FT-IR spectroscopy and single-crystal X-ray diffraction. The noncovalent interactions occurring in the crystal packing of both the complexes have been well-defined focusing on π···π (for complex **1**) and anion···π (for complex **2**) interactions, which have also been analysed using DFT calculations. Besides, noncovalent interactions such as C–H···π, lone pair···π, π···$\pi^+$, anion···$\pi^+$, and $\pi^+$···$\pi^+$ along with hydrogen bonding interactions play an important role in the stabilization of both the complexes in a solid state. We also observed that the change in auxiliary ligands exhibits significant variations in their structures, band gaps and photoresponse properties. To gain insights into the charge transport mechanism, several Schottky barrier diode (SBD) parameters like carrier mobility, transit time, carrier concentration, diffusion coefficient, diffusion length, and ideality factor were measured in the light of thermionic emission and SCLC (space charge limiting current) theory.

## Introduction

Recently, the fields of coordination chemistry and crystal engineering have matured enough and crystal engineering techniques have been extensively developed and assisted to the design and synthesis of materials with precise solid-state intriguing properties.[1,2] Researchers are now focusing on their potential applications as functional materials for use in heterogeneous catalysis, nanotechnology, gas adsorption, gas evolution, optoelectronics, drug delivery, sensors, fuel cell, dye degradation and many more beyond their syntheses.[3–11] In this context, crystal engineers often help to analyze the self-assembly process after a combination of various metals and heterocycle-based organic ligands and guide to find out the relationship between the structure and properties of molecules in a programmed way.[12]

Coordination molecular architectures are the result of mutual interactions to exhibit a broad range of different dimensional frameworks (0D, 1D, 2D or 3D) by a variety of forces.[13] Apart from coordination bonding interactions, forces associated with aromatic–π systems like π···π, lone pair···π, π···cation, π···anion, CH···π, anion···$\pi^+$, π···$\pi^+$, $\pi^+$···$\pi^+$, *etc.* along with relatively strong hydrogen bonding have been vastly scrutinized for the building of various polymeric architectures in the solid state.[14–16] Counter ions, solvent molecules and the electronic nature of ancillary ligands are also responsible for the organised ultimate architectures.[17]

2,4,6-Tri(pyridin-2-yl)-1,3,5-*s*-triazine and their structural analogues play a pivotal role in metallo-supramolecular chemistry and have drawn much attention in the fields of coordination chemistry and materials science.[18] The chelating aptitude of 2,4,6-tri(pyridin-2-yl)-1,3,5-*s*-triazine boosts the stability of metal complexes, and the planarity of the ligand with π stacking ability leads to robust intercalative interactions of complexes in biological systems.[19] The binding constant determines the strength of the interaction between the metal and the ligand and controls the formation of coordination molecules thermodynamically,[20] and a competition might arise if more than one ligand is present to bind with a specific metal ion. Thus, there is a smaller number of complexes reported in the literature with two different chelating ligands in one pot.[21] In addition, a majority of coordination

[a] *Department of Chemistry, Jadavpur University, Kolkata 700032, India. E-mail: ju_subrata@yahoo.co.in*
[b] *Department of Chemistry, Haldia Government College, Debhog, PurbaMedinipur, West Bengal, India*
[c] *Departament de Química, Universitat de les Illes Balears, Crta. de Valldemossa km 7.5, 07122 Palma de Mallorca, Baleares, Spain. E-mail: toni.frontera@uib.es*

† Electronic supplementary information (ESI) available: Crystal data, refinement parameters, geometric details, Tables S1–S10 and Fig. S1–S10. CCDC 2052737 and 2052738. For ESI and crystallographic data in CIF or other electronic format see DOI: 10.1039/d1nj01363g



 

compounds are electrical insulators and discrete in nature. However, there are some reports of ordered coordination compounds that show enhanced electron transport and rectifying nature under light illumination.[22–24] It is demonstrated that the structural and electronic properties of coordination compounds can be tuned by changing metal ions and organic linkers. As the conductivities of coordination compounds are generally low, the fabrication of electronic devices becomes a challenge when using these compounds. Beyond structural stability, thermal stability and chemical stability are also considered for the successful implementation of coordination compounds in device making. Considering the above facts, we have synthesised two nickel complexes based on the 2,4,6-tri(pyridin-2-yl)-1,3,5-*s*-triazine moiety. Initially, nickel(II) reacts with two different ligands (2,4,6-tri(pyridin-2-yl)-1,3,5-*s*-triazine and pyridine-2,6-dicarboxylic acid) in one pot to obtain an octahedral complex **1** where the triazine moiety and pyridine-2,6-dicarboxylic acid act as tridentate ligands. The unprecedented formation of complex **1** with two different chelating ligands is also established theoretically through the formation of a four-component assembly of complex **1**. When Ni(II) is treated with 2,4,6-tri(pyridin-2-yl)-1,3,5-*s*-triazine only as a ligand in the molar ratio of 1 : 2, the octahedral complex **2** was obtained. Although a number of complexes built from *s*-triazine derivatives have been reported in recent years, there still remains much more work to be explored. The structural features and supramolecular aspects of complexes **1** and **2** with the help of a single-crystal X-ray diffraction study along with their electrical conductivities have been investigated. The solid-state structure of complex **1** comprises a combination of C–H···N, C–H···O, C–H···Cl, N–H···O, O–H···O and O–H···Cl hydrogen bonds along with π···π, π···$\pi^+$ and lone pair···π interactions. Complex **2** is stabilized by a combination of C–H···F, N–H···O and O–H···F hydrogen bonds along with π···π, C–H···π, anion···π, $\pi^+$···$\pi^+$ and anion···$\pi^+$ interactions. To further understand the charge transportation, a detailed *I–V* analysis is carried out by making thin films of precursor complexes. Several device parameters like carrier mobility, carrier concentration, transit time, diffusion coefficient, diffusion length, and ideality factor have been measured by considering the SBD characteristics. The change in ancillary ligands alters the structural variations, supramolecular behaviours and electrical properties of both the complexes. An improvement in device performance was observed for complex **2** compared to complex **1**.

# Experimental section

### Physical measurements

Elemental analyses (C, H and N) were performed using a PerkinElmer 2400 Series-II CHN analyzer. Fourier transform-infrared (FT-IR) spectra of complexes **1** and **2** were recorded using a PerkinElmer LX-1 FTIR spectrophotometer (4000–400 $cm^{-1}$) by using a modern diamond attenuated total reflectance (ATR) accessory method. UV–vis absorption spectra were obtained using a UV-1700 PharmaSpec UV–vis spectrophotometer (SHIMADZU). The electrical characterization was carried out using a Keithley 4200 *I–V* instrument in the voltage range of −1 to +1 V. Single-crystal X-ray data collections of complex **1** (Fig. S1, ESI†) and complex **2** (Fig. S2, ESI†) were completed using a single-crystal X-ray diffractometer (Bruker Smart Apex II).

### Materials

All chemicals [2,4,6-tri(pyridin-2-yl)-1,3,5-*s*-triazine, dipicolinic acid, Ni(II) chloride hexahydrate, and ammonium hexafluorophosphate] were purchased from Sigma-Aldrich Chemical Company, USA and used as received. All reactions were carried out under aerobic environments and doubly distilled water was used throughout (Scheme S1, ESI†).

### Synthesis of complex 1

Nickel(II) chloride hexahydrate (0.237 g, 1.0 mmol) was dissolved in 15 mL of water and allowed to react with 2,4,6-tri(pyridin-2-yl)-1,3,5-*s*-triazine (0.312 g, 1.0 mmol) in the water–ethanol (8 : 2, v/v) medium (20 mL) at 60 °C by continuous stirring. A warm aqueous solution (15 mL) of dipicolinic acid (0.334 g, 2.0 mmol) was added dropwise to the above solution under stirring conditions. After 4 h of constant stirring at 60 °C, the resultant solution was cooled, filtered and left unperturbed for slow evaporation at room temperature. Block-shaped brown-colored single crystals were obtained after one week. The crystals were separated by filtration, washed with cold water, and then dried in air, to obtain a 65% yield (0.495 g). Anal. calcd. for $C_{32}H_2N_8NiClO_9$ (complex **1**): C, 51.96; H, 2.86; and N, 15.15%. Found: C, 51.92; H, 2.81; and N, 15.14%. Main FT-IR absorption (KBr, $cm^{-1}$): 3364 (w), 3097 (vs), 2781 (s), 2621 (s), 1727 (vs), 1621 (s), 1573 (s), 1557 (vs), 1480 (s), 1453 (s), 1429 (s), 1400 (s), and 1384 (s) (Fig. S3, ESI†).

### Synthesis of complex 2

Complex **2** was synthesized by dissolving nickel(II) chloride hexahydrate (0.237 g, 1.0 mmol) in 15 mL of water and allowed to react with 2,4,6-tri(pyridin-2-yl)-1,3,5-*s*-triazine (0.624 g, 2.0 mmol) in the water–ethanol (8 : 2, v/v) medium (20 mL) at 60 °C by stirring. A few drops of HCl were added into the resultant turbid solution to obtain the clear solution. A warm aqueous solution (15 mL) of ammonium hexafluorophosphate (0.652 g, 4.0 mmol) was added dropwise to the above solution and stirred for another 3 h. The resultant solution was then cooled, filtered, and left for slow evaporation at room temperature without any disturbance. Block shaped, deep brown-colored single crystals were obtained after two weeks. The crystals were separated by filtration, washed with cold water and air dried, to obtain a 62% yield (0.796 g). Anal. calcd. for $C_{36}H_{28}N_{12}NiOF_{24}P_4$ (complex **2**): C, 34.17; H, 2.07; and N, 13.28%. Found: C, 34.21; H, 2.04; and N, 13.23%. Main FT-IR absorption (KBr, $cm^{-1}$): 3454 (w), 3031 (s), 1740 (s), 1635 (s), 1611 (s), 1578 (vs), 1562 (vs), 1530 (vs), 1487 (s), 1473 (s), 1455 (s), 1439 (s), 1399 (s), 1377 (s), and 1313 (s) (Fig. S3, ESI†).

### Theoretical methods

The calculations of monomers and dimers (Fig. 7–9) were performed at the DFT level of theory using the PBE0[25]–D3[26] method and the def2-SVP basis set,[27] with the help of the

Gaussian-16 program.[28] The topological analysis of the electron density distribution has been examined using the noncovalent interaction plot (NCI plot)[29–31] using the AIMAll program.[32] The estimation of the individual XB energies was performed using the potential energy density ($V_r$) predictor as recently proposed in the literature ($E = 0.778V_r$)[33] for the PBE0 functional. MEP surfaces were computed at the same level of theory by means of the Gaussian-16 program.

## Results and discussion

### X-Ray crystallographic analysis

Single-crystal X-ray data collections for both the complexes were performed using a Bruker SMART APEX II CCD area detector equipped with a graphite-monochromated Mo Kα radiation (λ = 0.71073 A) source in φ and ω scan modes at 273(2) K. The cell parameter refinement and data reduction were carried out using the Bruker SMART APEX II instrument and Bruker SMART and Bruker SAINT Software[34] for both the complexes. The structure of both the complexes was solved by conventional direct methods and refined by full matrix least-squares methods using $F^2$ data. SHELXL-2014/7[35] was used for the solution and refinement of both the structures. The solvent masking method in the Olex-2 programme was used for complexes **1** and **2** to obtain better fitted models of data. CCDC 2052738 (for complex **1**) and 2052737 (for complex **2**) include additional crystallographic information. Selected crystal data and structure refinement parameters for complexes **1** and **2** are given in Table S1 (ESI†).

### Structural description of complex 1

The single-crystal X-ray diffraction study shows that the asymmetric unit of complex **1** comprises one monomeric cationic $[Ni(C_{18}H_{13}N_6)(C_7H_3NO_4)]^+$ unit, one non-coordinated dipicolinic acid, one non-coordinated chloride ion and one non-coordinated water molecule (Fig. S1, ESI†). The complex adopts the triclinic system with the space group $P\bar{1}$ and its unit cell is composed of two asymmetric units. The selected bond lengths and bond angles are tabulated in Tables S2 and S3 (ESI†). In the monomeric cationic $[Ni(C_{18}H_{13}N_6)(C_7H_3NO_4)]^+$ unit, the Ni(II) ion occupies the distorted octahedron structure, where three nitrogen donor atoms (N13, N30 and N36) of triazine-based ligand and another nitrogen atom (N9) of dipicolinate construct the basal plane. Two oxygen atoms O1, at a distance of 2.170(3) Å, and O12, at a distance of 2.109(3) Å, of the same acid ligand are *trans* diaxially coordinated to the metal ion. The lower value of the *trans* axial angle O1–Ni1–O12 [155.94(11)°] induces distortion in the octahedral geometry. The Ni–N bond distances in the basal plane are in the range of 1.960(3) to 2.140(3) Å. The Ni(II) ion is almost placed (deviation, 0.009 Å) in the same mean coordination plane of (N13, N30, N36, and N9). The one N atom (N27) of the monomeric unit is protonated. A non-coordinated chloride anion is present to neutralize the charge of the complex.

The monomeric cationic unit of complex **1** extends to make certain a 1-D polymeric chain through the π···π interaction (Table S5, ESI†) between Cg(6) and Cg(9) of two units along the [100] direction (Fig. S4, ESI†). The two parallel chains are then interconnected through the self-complementary π···$\pi^+$ interaction (Table S5, ESI†) between Cg(9) of one unit and Cg(8) of the other unit, thus forming a 1-D tape (Fig. S5, ESI†). The ring centroid separation distances of Cg(6)–Cg(9) and Cg(8)–Cg(9) are 3.715(3) Å and 3.561(3) Å, respectively. This supramolecular architecture is further extended through the self-complementary lone pair···π interactions (Table S7, ESI†) between Cg(5) of one unit and the carboxyl oxygen atom (O11) of the other unit and *vice versa*. Thus, the π···π interaction along with these π···$\pi^+$ and lone pair···π interactions enhances the dimensionality from 1-D to 2-D in the (101) plane (Fig. 1).

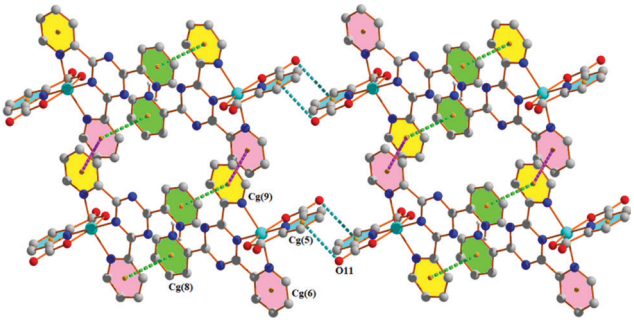


Fig. 1 2-D layer of complex **1** incorporating π···π, π···$\pi^+$ and lone pair···π interactions (aromatic hydrogen atoms have been omitted for clarity).

A different 2-D layer is fashioned in complex **1** using two different types of hydrogen bonding interactions (Table S4, ESI†). Here, two monomeric cationic units are connected through C5–H5···O48 (154°) and O37–H37···O11 (164°) hydrogen bonds for the propagation of a one-dimensional (1-D) polymeric chain that is further strengthened by the C43–H43···O3 (149°) hydrogen bond, thus forming a $R_2^2(10)$ ring motif. These parallel 1-D chains are interlinked using the C25–H25···O47 (149°) hydrogen bonding interaction to form a 2-D layer (brick wall like) in the (011) plane (Fig. 2).

A comprehensive analysis reveals that four different types of intermolecular hydrogen bonding interactions (C–H···O, C–H···Cl, N–H···O, and O–H···Cl) are involved in the formation

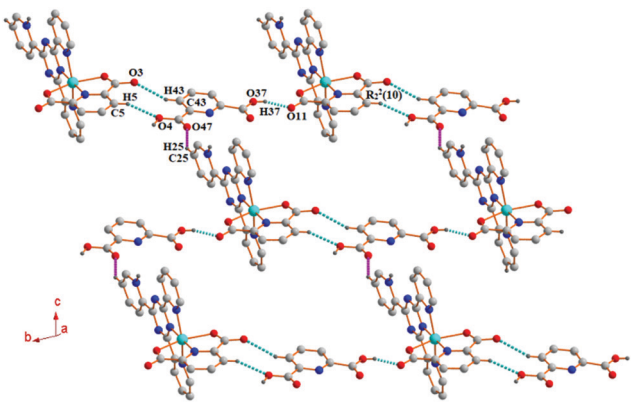


Fig. 2 Perspective view of the 2-D layer of complex **1** incorporating H-bonding interactions (other aromatic hydrogen atoms have been omitted for clarity).

 

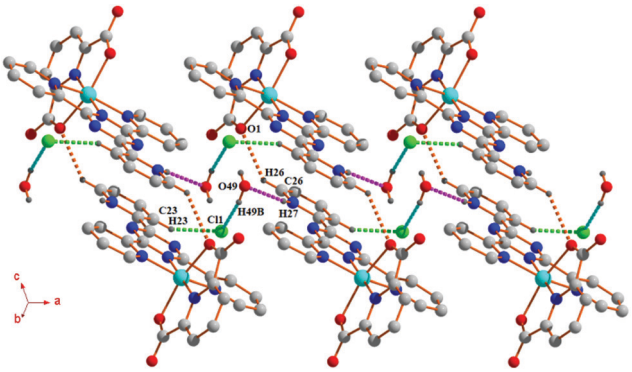


Fig. 3 Formation of 1-D tape through hydrogen bonding interactions in complex **1** (other aromatic hydrogen atoms have been omitted for clarity).

of a 1-D tape (as shown in Fig. 3). The first type of intermolecular hydrogen bonding (shown by green dotted lines) was shaped between the C23–H23 of one monomeric cationic unit and the non-coordinated chlorine atom (Cl1). The second type of intermolecular hydrogen bonding (shown by aqua dotted lines) was formed by the O49–H49B of the non-coordinated water molecule and the non-coordinated chlorine atom (Cl1). The third type of intermolecular hydrogen bonding (shown by pink dotted lines) was formed by the N27–H27 of one unit and O atom (O49) of the non-coordinated water molecule. These three hydrogen bonding interactions played a significant role to form a one-dimensional (1-D) polymeric chain along the [100] direction. The two parallel chains are then interconnected through the self-complementary C26–H26···O1 (type four) bonds (shown by orange dotted lines) for the formation of 1-D tape (Fig. 3).

In complex **1**, a dimeric distribution is observed that is formed by the π···π interaction between Cg(5) of one monomeric cationic unit and Cg(10) of the non-coordinated dipicolinic acid (Fig. S6, ESI†). The dimeric integrity is further stabilized through carbonyl (lp)···π and C35–H35···N45 hydrogen bonding interactions. Here, the carbonyl oxygen atom (O47) approaches the π face of the Cg(1) chelate ring at $(2-x, 1-y, 1-z)$ to form the said (lp)···π interaction. Then, another carbonyl oxygen atom (O39) interacts simultaneously with Cg(1) and Cg(5) of the adjacent dimeric unit to form a 1-D polymeric chain which is further strengthened by the C14–H14···O39 hydrogen bond.

### Structural description of complex 2

The asymmetric unit of complex **2** contains one monomeric cationic $[Ni(C_{18}H_{13}N_6)_2]^{4+}$ unit, four non-coordinated hexafluorophosphate anions and one non-coordinated water molecule (Fig. S1, ESI†). The complex crystallizes in the triclinic system having the space group $P\bar{1}$ and its unit cell consists of two asymmetric units. The selected bond lengths and bond angles are summarized in Table S2 and S3 (ESI†), respectively. In this monomeric cationic $[Ni(C_{18}H_{13}N_6)_2]^{4+}$ unit, the Ni(II) ion possesses a distorted octahedron where the six coordination mode around the metal centre is satisfied by six N atoms (N1, N18, N24, N25, N36 and N47) from the two triazine-based ligands. The four N atoms (N1, N18, N24 and N36) are involved to construct the basal plane and another two N atoms (N25 and N47) are axially coordinated to the metal ion. The Ni–N distances in the basal plane are in the range of 1.990(4) to 2.177(4) Å. The *trans* angle, N25–Ni1–N47, is distorted with a value of 152.86(17)° and the metal ion almost lies (deviation, 0.01 Å) in the mean coordination plane of (N25, N36, N47, and N18). Two nitrogen atoms (N15 and N35) in the monomeric unit of complex **2** are protonated. These two monopositively charged N-centers along with a Ni(II) ion induce the overall tetra-positive charge, which is compensated by four noncoordinated hexafluorophosphate anions.

The monomeric cationic unit of complex **2** propagates to make certain a 1-D polymeric chain through the π···π stacking interaction (Table S5, ESI†) between Cg(9) and Cg(12) of two different units along the [100] direction having a separation distance of 3.957(3) Å (Fig. S7, ESI†). This 1-D array is further extended to 2-D layers through the C–H···π interaction at $(x, -1+y, z)$ (Table S6, ESI†) between C4–H4 of one unit with Cg(9) of the other unit in the (110) plane (Fig. 4).

A different 2-D layer (Fig. 5) is constructed in complex **2** by using hydrogen bonding, $\pi^+\cdots\pi^+$, and anion···π (Table S7, ESI†) interactions. Here, two monomeric cationic units are connected through anion···π interactions *via* two F atoms (F19 and F23) with Cg(5) and Cg(12) of the first unit, respectively, and one F atom (F24) with Cg(10) of the second unit for the propagation of a one-dimensional (1-D) polymeric chain that is again interconnected by the self-complementary C38–H38···F1 and C44–H44···F6 hydrogen bonds (Table S4, ESI†), thus forming a 1-D tape. This 1-D tape is further extended to 2-D layers (011) through the $\pi^+\cdots\pi^+$ interaction between Cg(7) of one unit with

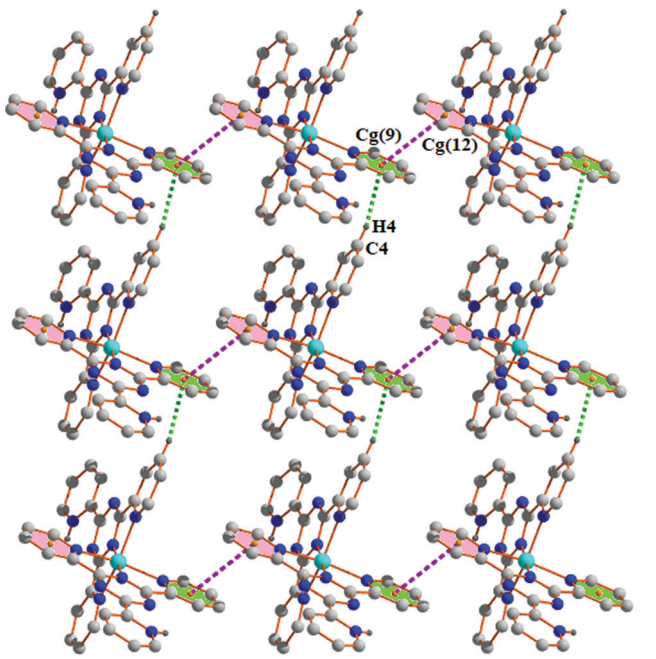


Fig. 4 Perspective view of the 2-D layer generated through π···π and C–H···π interactions in complex **2** (other aromatic hydrogen atoms have been omitted for clarity).

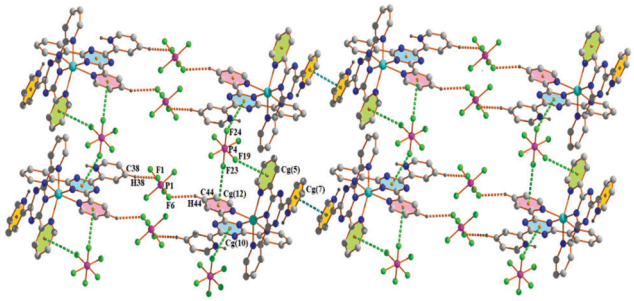

Fig. 5 Perspective view of 2-D architecture incorporating anion···π/$\pi^+$···$\pi^+$/hydrogen bonding interactions in complex **2** (other aromatic hydrogen atoms have been omitted for clarity).

Cg(7) of the other unit having an inter-planar spacing of 3.635(4) Å (Table S5, ESI†).

In addition, one-dimensional (1-D) tape is formed in complex **2** using anion···π (Table S4, ESI†) and hydrogen bonding interactions (Table S4, ESI†). Firstly, monomeric cationic units are connected through anion···π interactions *via* one F atom (F15) with Cg(6) of one unit and one F atom (F17) with Cg(5) of the other unit for the propagation of a one-dimensional (1-D) polymeric chain along the [100] direction. Due to the self-complementary nature, the two parallel chains are interlinked through another anion···π interaction *via* one F atom (F9) with Cg(8) of one monomeric unit and three hydrogen bonding [P2–F10···O2, P2–F12···O2 and N15–H15···H2B] interactions, thus resulting in a 1-D tape (as shown in Fig. 6).

Another two-dimensional (2-D) layer (Fig. S8, ESI†) is formed in complex **2** using anion···π and anion···$\pi^+$ (Table S7, ESI†) interactions. Here, monomeric cationic units are connected through anion···π interactions *via* one F atom (F22) with Cg(5) of the first unit and Cg(10) of the second unit for the propagation of a one-dimensional (1-D) polymeric chain. Now, this 1-D

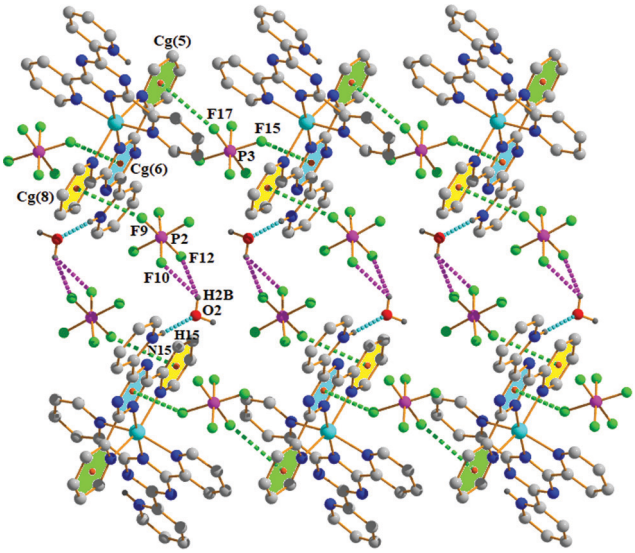


Fig. 6 Perspective view of 1-D tape generated through incorporating anion···π and hydrogen bonding interactions in complex **2** (aromatic hydrogen atoms have been omitted for clarity).

chain is further extended to 2-D layers (110) through another anion···π interaction [*via* one F atom (F17) with Cg(5) of one unit] and anion···$\pi^+$ interaction [*via* one F atom (F18) with Cg(7) of the other unit].

Again, the crystal structure of **2** reveals the existence of various intermolecular hydrogen bonding (Table S4, ESI†) interactions in the solid state leading to the organization of a one-dimensional (1-D) zigzag polymeric chain along the [001] direction (Fig. S9, ESI†). Here, two monomeric cationic units are interconnected through the self-complementary C13–H13···F13, C14–H14···F18, C45–H45···F17 and C46–H46···F15 hydrogen bonds (shown as green dotted lines); thus generating two different $R_2^2(7)$ ring motifs. Now these dimeric units are repeated in a zigzag fashion *via* another two intermolecular hydrogen bonding [C2–H2···F6 and C39–H39···F4] interactions which are self-complementary in nature (shown in pink dotted lines).

## DFT calculations

The theoretical study is focused on the analysis of π-stacking assemblies in complex **1** and anion···π interactions in complex **2**. Fig. 7a shows a partial view of the X-ray structure of complex **1** where the π···π/π···π/π···π four-component assembly is highlighted.

Two different types of π-stacking are formed: (i) a non-conventional one, denoted as $(\pi\cdots\pi)_1$, established between two non-coordinated dipicolinic acids, where the exocyclic carboxylic group of one ligand interacts with the π-cloud of the adjacent ligand, and *vice versa* (denoted as homodimer B as shown in Fig. 7c). (ii) A conventional one, denoted as $(\pi\cdots\pi)_2$, where the aromatic rings of the coordinated and non-coordinated dipicolinic acids interact (denoted as heterodimer A as shown in Fig. 7a). The latter is expected to be stronger due to the larger polarization of the π-system as a consequence of the coordination of the ligand to the Ni(II) metal center. The formation energy of this four-component assembly is very large ($\Delta E_{assembly} = -52.4$ kcal mol$^{-1}$), thus confirming the relevance of cooperative π···π/π···π/π···π interactions in the solid state of complex **1**. In order to compare both types of π-stacking and also the existence of cooperativity effects, we have performed additional calculations, which are summarized in Fig. 7b and c. It can be observed that the interaction energies of heterodimer **A** (Fig. 7b) and homodimer **B** (Fig. 7c) are $\Delta E_{heterodimerA} = -20.6$ kcal mol$^{-1}$ and $\Delta E_{homodimerB} = -10.4$ kcal mol$^{-1}$, respectively, thus confirming the fact that the $(\pi\cdots\pi)_2$ binding mode is stronger. This larger dimerization energy is also due to the formation of a trifurcated H-bond between one aromatic C–H group and two O-atoms and one N-atom of dipicolinic acid (see dashed lines in Fig. 7b). In order to investigate the existence of cooperativity effects, we have also computed the formation energy of the four-component assembly by using heterodimer **A** as the starting point, which is $\Delta E_1 = -11.0$ kcal mol$^{-1}$. The comparison of this formation energy with the one of homodimer **B** ($\Delta E_{homodimerB} = -10.4$ kcal mol$^{-1}$) gives information about the influence of $(\pi\cdots\pi)_2$ on the strength of $(\pi\cdots\pi)_1$. Consequently, $(\pi\cdots\pi)_1$ is reinforced by 0.6 kcal mol$^{-1}$ due to its coexistence with $(\pi\cdots\pi)_2$, thus confirming the existence of cooperativity effects. Similarly, we have also computed the

 

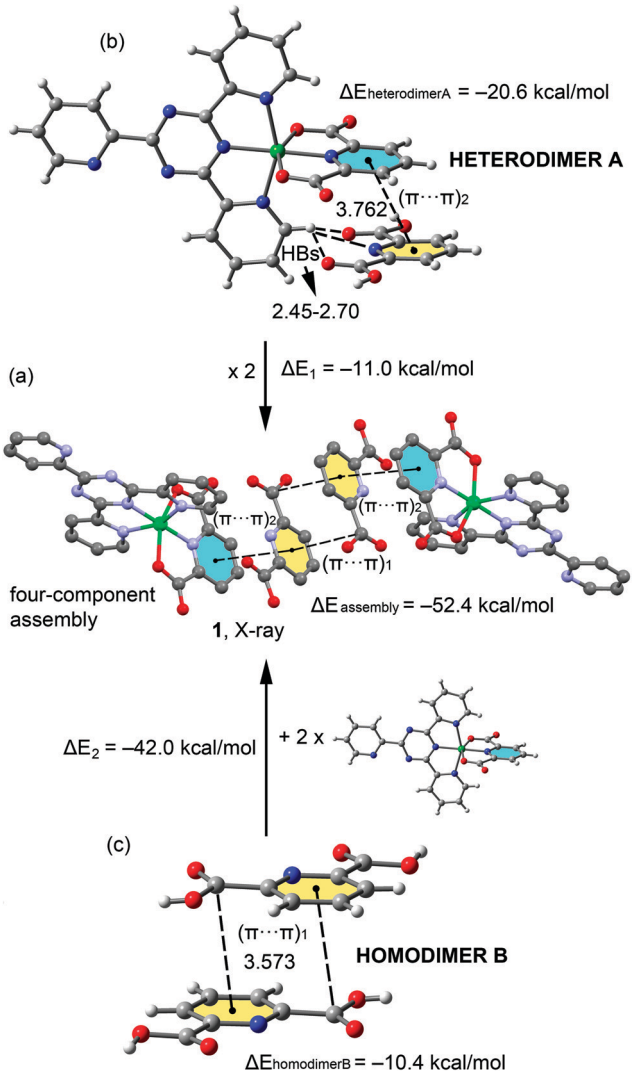


Fig. 7 (a) Partial view of the X-ray structure of complex **1**. H- atoms have been omitted for clarity. (b and c) Theoretical models used to evaluate the interaction energies. Distances are in Å.

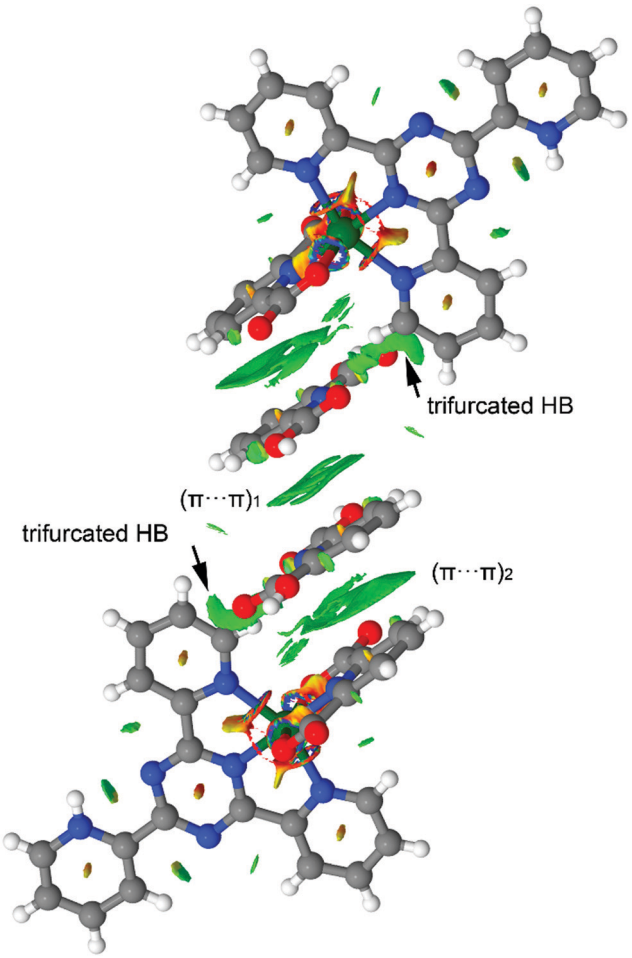


Fig. 8 NCI plot of the four-component assembly of complex **1**. Isosurface of 0.4 a.u; density cut-off of 0.04 a.u. Colour scale −0.035 a.u. ≤ sign($\lambda_2$)$\rho$ ≤ 0.035 a.u.

formation energy of the four-component assembly by using homodimer **B** as the starting point. The formation energy is $\Delta E_2 = -42.0$ kcal mol$^{-1}$ which accounts for two symmetrically equivalent $(\pi\cdots\pi)_2$ interactions. The comparison of this interaction energy with twice the dimerization energy of heterodimer **A** ($2 \times \Delta E_{\text{heterodimerA}} = -41.2$ kcal mol$^{-1}$ reveals that the $(\pi\cdots\pi)_2$ interactions are reinforced by 0.8 kcal mol$^{-1}$ as a consequence of the presence of $(\pi\cdots\pi)_1$.

We have further used the noncovalent interaction plot index (NCI plot) to characterize the $\pi\cdots\pi/\pi\cdots\pi/\pi\cdots\pi$ assembly in complex **1**. The NCI plot is an intuitive method that shows which spatial regions interact between molecules. Consequently, it is very convenient to analyse noncovalent interactions. Moreover, it gives hints regarding the strength of interactions by using a colour code, where green is used for weak interactions and yellow for repulsive ones. Strongly attractive and repulsive interactions are represented by blue and red colours, respectively. The NCI plot of the four-component assembly is given in Fig. 8, which confirms the existence of $\pi\cdots\pi$ stacking interactions that are characterized by large and green isosurfaces. In the case of $(\pi\cdots\pi)_1$, the isosurfaces embrace the carboxylic groups, thus confirming their participation in the π-stacking interaction. In the case of the $(\pi\cdots\pi)_2$ binding mode, the isosurface is more extended, confirming a larger overlap of the π-systems. Moreover, the existence of the trifurcated C–H···O, N, O interaction is also confirmed by the presence of a green isosurface located between the H-atom and the three electron donor atoms belonging to dipicolinic acid.

Finally, we have also studied anion···π interactions observed in the solid state of complex **2** by using the NCI Plot index as shown in Fig. 11. The NCI plot representation shows that up to six $PF_6^-$ anions concurrently form anion–π interactions with the extended and π-acidic rings of the Ni(II)-coordinated 2,4,6-tri(pyridin-2-yl)-1,3,5-*s*-triazine ligands. Due to the protonation of the ligand, the anion···π interactions are very strong. We have evaluated two of them as representative contacts (see Fig. 9) and the interaction energies are −98.4 and −89.2 kcal mol$^{-1}$, which are in the range of previously reported anion–$\pi^+$ interactions.[36]

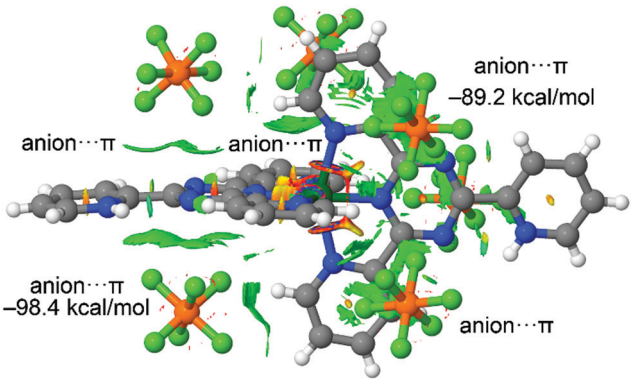


Fig. 9 NCI plot of complex **2** surrounded by six $PF_6^-$ anions establishing anion–π interactions. Isosurface of 0.4 a.u; density cut-off of 0.04 a.u. Colour scale −0.035 a.u. ≤ sign($\lambda_2$)$\rho$ ≤ 0.035 a.u.

### Optical studies

UV–vis absorption spectra were used to calculate the band gap of complexes and to know the type of absorption. Fig. 10(a) and (b) shows UV–vis absorption spectra of complexes **1** and **2,** respectively. Almost similar sharp visible range absorptions are observed for both complexes. To calculate the band gap energy conventional Tauc's relation was used

$$(\alpha h\nu) \propto (h\nu - E_g)^n \quad (1)$$

where $\alpha$ represents the absorption coefficient; $h\nu$ is the photon energy; $E_g$ represents the band gap of materials and coefficient '$n$' is for direct band-to-band transition having a value of 1/2. Now plotting $(\alpha h\nu)^2$ *vs.* $h\nu$ and extrapolating the linear portion of the curve gives the corresponding optical band gap values of the complexes. The band gaps ($E_g$) were calculated as 3.89 and 3.76 eV for complexes **1** and **2,** respectively and they are shown in the inset of Fig. 10. The wide band gap of both complexes falls under the semiconductor regime and is an indication of their device making properties.

### Fabrication of the thin film and FTO/complex/Ag junction

The prime criterion of device making is the small size of the synthesized materials. As the thin film technology bridges in between macro systems and molecular systems where the size of the material is substantially reduced and is welcomed for device fabrication. With this simplification, precursor complexes are turned into thin films. Here, both precursor complexes were taken into account to deposit on FTO substrates (resistance 8–10 Ω $cm^{-2}$ and surface area 1.0 × 1.0 $cm^2$) by a spin-coating method. Before the deposition, FTO substrates were properly washed, first with soap-water and then with running distilled water. After this, they were ultrasonicated for an hour and degreased, and thereafter, they were shifted in a hot air oven for proper drying (almost 2 hours). About 4 mg of each complex was then dispersed in DMF in a 1 : 5 ratio and ultrasonicated again for an hour. Now with a micropipette, a few drops of this solution were added onto the centre of FTO and spun at 700 rpm and then 1000 rpm for 2 and 4 minutes, respectively. The resulting films were dried in an inert atmosphere and kept in desiccators. The thicknesses of the films were measured to be 2 μm using a surface profilometer (Bruker Contour G). To fabricate the sandwich device, two contacts were made one from FTO (bottom contact) and the other from the contact metal Ag (FTO/complex/Ag) and a shadow mask was used to maintain an effective area of 7 × $10^{-2}$ $cm^2$.

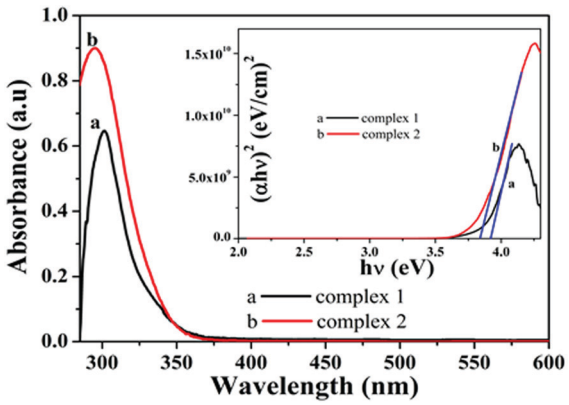


Fig. 10 UV–vis spectrum of (a) complex **1** inset: band gap of complex **1** (b) complex **2** and inset: band gap.

### Electrical measurements

Electrical measurements were performed at room temperature under dark and illumination conditions (sun light) in the voltage range of −1 to +1 V. Fig. 11 represents the characteristics current–voltage (*I–V*) curves of devices under dark and illumination conditions. The *I–V* nature of both complexes shows the non-linear rectifying nature which indicates that the materials are of p type and that they form the Schottky junction with the n type FTO substrate. The nature of the *I–V* curve represents the rectifying behaviour, similar to the Schottky barrier diode (SBD). This indicates that the rectifying nature is highly influenced under illumination of incident radiation. The current rectification values, *i.e.* the on/off ratio of device 1 under dark and photo-illumination conditions, were found to be 2.95 and 31.31 at ±1 V, respectively, whereas for device 2, the rectification values enhanced to 31.32 and 54.93 under dark and illumination conditions, respectively. The conductivity measurement of the devices further indicates the enhanced electron transportation properties of device 2 under light conditions. Room temperature conductivity for device 1 was calculated to be 2.4 × $10^{-6}$ S $cm^{-1}$ and 6.0 × $10^{-6}$ S $cm^{-1}$ under dark and light conditions, respectively, whereas for device 2 under the same conditions, the conductivity increased to 1.48 × $10^{-5}$ S $cm^{-1}$ and 3.24 × $10^{-5}$ S $cm^{-1}$, respectively. The outcome indicates the significant photoresponse of device 2 compared to device 1.

To investigate the predominant charge transportation mechanism, these *I–V* curves must be carefully analysed. The non-linear *I–V* nature of the devices arises due to different types of charge transportation mechanisms and can be explained by the established model of Richardson–Schottky or Poole–Frankel.[37] Thermal activation of electrons over the metal-semiconductor interface results in Schottky emission in the presence of an applied field.[38] To obtain a clear understanding of the charge transport mechanism, thermionic emission theory has been

 

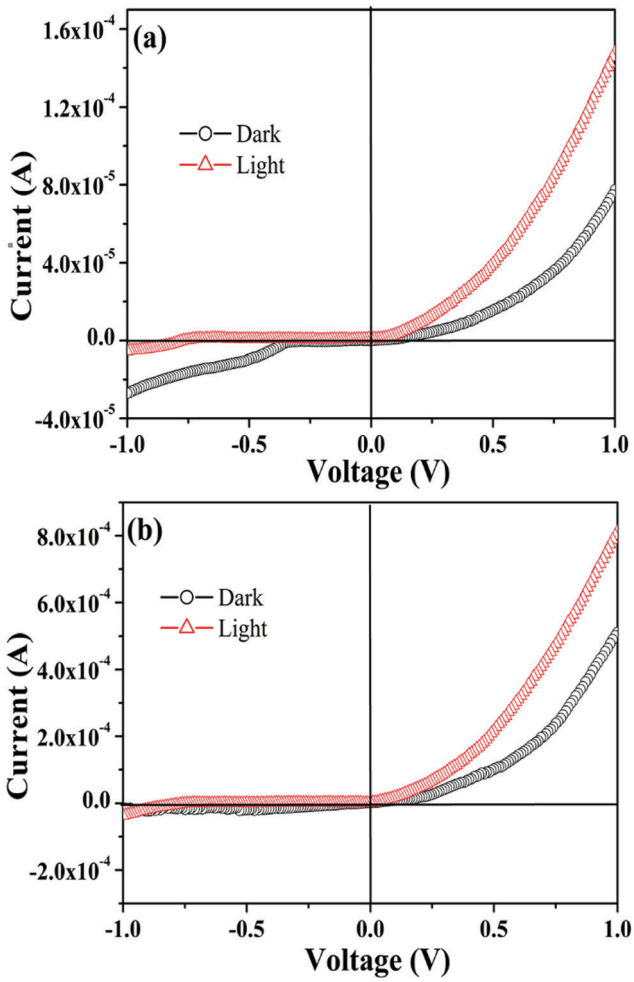


Fig. 11 *I–V* characteristic curve of (a) device 1 under dark and illumination conditions and (b) device 2 under dark and illumination conditions.

adapted to quantitatively analyse the *I–V* plots, where device parameters were confirmed by the Cheung's standard equation[39]

$$I = I_0[\exp((qV)/(\eta kT)) - 1] \quad (2)$$

Here, $I$ and $I_0$ are the forward and reverse saturation currents, $V$ and $q$ are the applied potential and electron charges, $k$ and $T$ are the Boltzmann constant and absolute temperature, and $\eta$ represents the ideality factor of SBD. The saturation current ($I_0$) can be expressed as

$$I_0 = AA^*T^2\exp[(-q\,\phi_B)/(KT))] \quad (3)$$

where the term $\phi_B$ represents barrier height; $A$ and $A^*$ are the diode area and Richardson constant, respectively. For both devices, the diode area was fixed as $7 \times 10^{-2}$ cm$^2$, and the effective Richardson constant was taken as 32 A K$^{-2}$ cm$^{-2}$. Now, *I–V* characteristics can also be represented as

$$I = I_0[\exp((q(V - IR_S))/(\eta kT))] \quad (4)$$

where the term $IR_S$ stands for the voltage drop across the series resistance and it can be calculated from the following equation:

$$dv/d(\ln I) = \eta KT/q + IR_S \quad (5)$$

Eqn (9) can also be expressed as a function of '$I$' by the following form

$$H(I) = IR_S + \eta\Phi_B \quad (6)$$

Hence, the series resistance ($R_S$) can be measured and calculated by the above two consecutive equations.

$H(I)$ can also be represented by the following equation

$$H(I) = V - (\eta KT/q)\ln(I/(AA^*T^2)) \quad (7)$$

Now using eqn (5), d$V$/d(ln$I$) *versus* $I$ (Fig. 12) is plotted to measure the series resistance ($R_S$) from the slope and ideality factor ($\eta$) from the intercept (under dark and light illumination conditions). The calculated ideality factor ($\eta$) values for device 1 are 2.81 and 1.79 under dark and light conditions, respectively, whereas for device 2, the $\eta$ values become 2.53 and 1.41 under the same conditions, respectively. Hence, with the irradiation of incident radiation, device 2 moves more towards ideality. The deviation of $\eta$ values from the ideality ($\eta$ = 1) is an indication of the improper metal–semiconductor junction which results from trapping states in the interface. The structural disorderliness of the compound plays a significant role; more clutter structures bring more trapping states and thereby easily deviate from the ideal value. There are some reports on the SBD device analysis that impose some other factors, like surface contamination, barrier tunneling, *etc.*, responsible for non-ideality.[40,41]

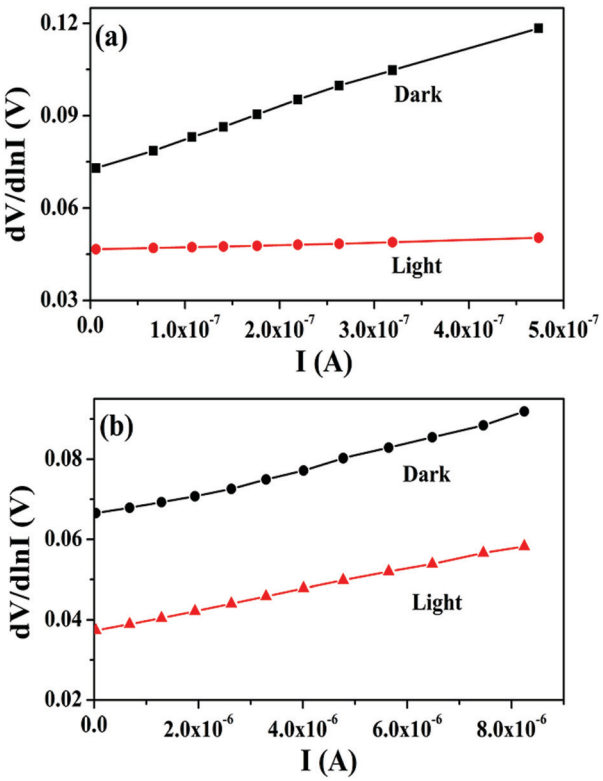


Fig. 12 d$V$/d(ln$I$) *vs.* $I$ plot under dark and illumination conditions for (a) device **1** and (b) device **2**.

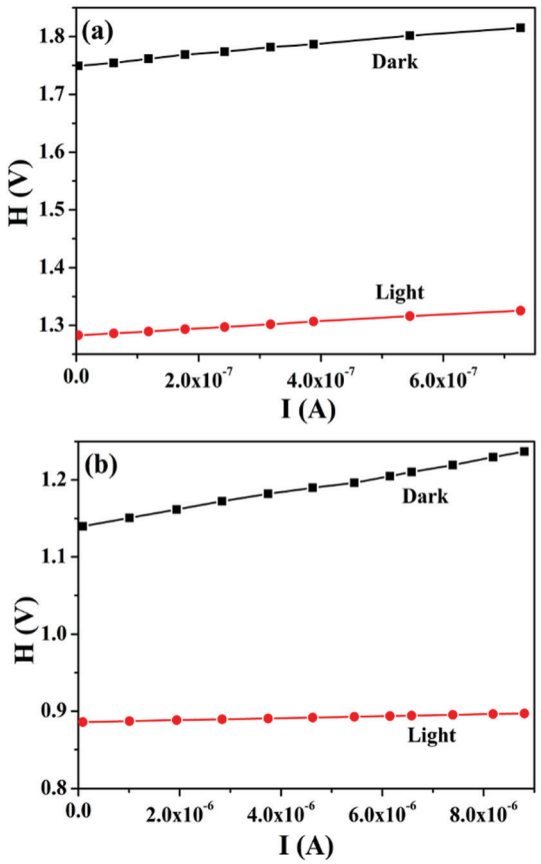


Fig. 13 *H* (*V*) *vs.* I plot under dark and illumination conditions for (a) device 1 and (b) device 2.

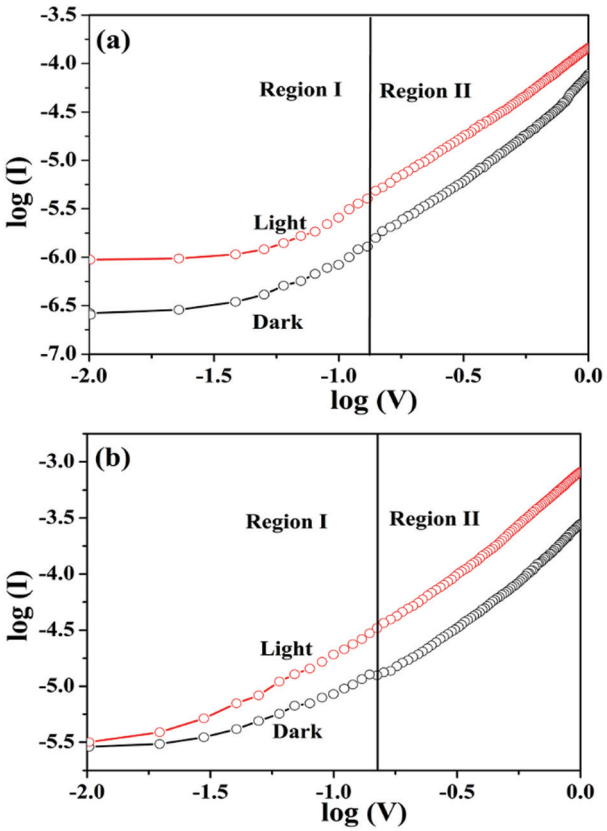


Fig. 14 log (*I*) *vs.* log (*V*) plot under dark and illumination conditions for (a) device 1 and (b) device 2.

The potential barrier height ($\Phi_B$) values are calculated from the intercepts of *H*(*V*) *vs. I* plot of both devices (Fig. 13) using eqn (6). The '*H*' values are calculated by means of $\eta$ values obtained from Fig. 12 using eqn (5).

To gain insights into the charge transport phenomenon of carrier transport through the interface of the MS junction, the log–log plot, *i.e.*, log(*I*) *versus* log(*V*), was analyzed (Fig. 14). The presence of two distinct regions in the log–log plot ensures different conduction mechanisms are operating here. Now applying the power law ($I \propto V^m$) (where $m$ is slope value) on the log–log plot, the governing mechanism prevailing in carrier conduction can be specified. By analyzing the slope value '$m$', two distinct zones can be separated, $m \geq 2$ indicates a space-charge-limited-current (SCLC) region whereas a value less than or equal to 1 ($m \leq 1$) indicates the ohmic zone.[42,43] Fig. 14 represents log (*I*) *vs.* log (*V*) plot of devices 1 and 2 in the absence and presence of light. The presence of two separate regions indicates that different conduction mechanisms are prevailing here. At region I, *i.e.*, at low bias voltage, the compound exhibits an ohmic nature ($I \propto V$). The *I*–*V* characteristic in this region can be imposed to thermionic emission. Just after this, the *I*–*V* curve obeys power law behaviour ($I \propto V^m$) and it is assigned as region II.

In region II, the current is ruled by the space charge limited current (SCLC) which is proportional to the square of the applied voltage ($I \propto V^2$).[44,45] This SCLC region gives several important device performances like carrier concentration ($N$), carrier mobility ($\mu_{eff}$), diffusion coefficient ($D$), diffusion length ($L_D$), transit time ($\tau$), *etc.*

Dielectric constants of the compounds were measured from the saturation capacitance ($C$) value of capacitance *vs.* frequency plot (Fig. S10, ESI†) by using the following equation.[46]

$$\varepsilon_r = (1/\varepsilon_0)(C \cdot L/A) \quad (8)$$

Here, $L$ is the thickness of the deposited material and $A$ is the diode area. The measured relative dielectric constants of the material were calculated to be 32.26 and 6.45 for complexes **1** and **2**, respectively. A comparatively low dielectric constant of complex **2** suggests its preferential use in power generation to minimize the electric power loss.

The effective carrier mobility ($\mu_{eff}$) of both devices has been calculated from the *I vs.* $V^2$ (Fig. 15) plot by employing the Mott–Gurney eqn (11)[47]

$$J = (9\mu_{eff}\varepsilon_0\varepsilon_r V^2)/(8d^3) \quad (9)$$

Here $J$ is the current density, $\varepsilon_0$ and $\varepsilon_r$ are the permittivity of vacuum and relative dielectric constant of compounds, respectively. The device made of complex **2** has a higher mobility ($5.36 \times 10^{-4}$ cm$^2$ V$^{-1}$ s$^{-1}$) than that of complex **1** ($3.19 \times 10^{-4}$ cm$^2$ V$^{-1}$ s$^{-1}$).

Other important device performances like carrier concentration ($N$), carrier mobility ($\mu_{eff}$), diffusion coefficient ($D$),

 

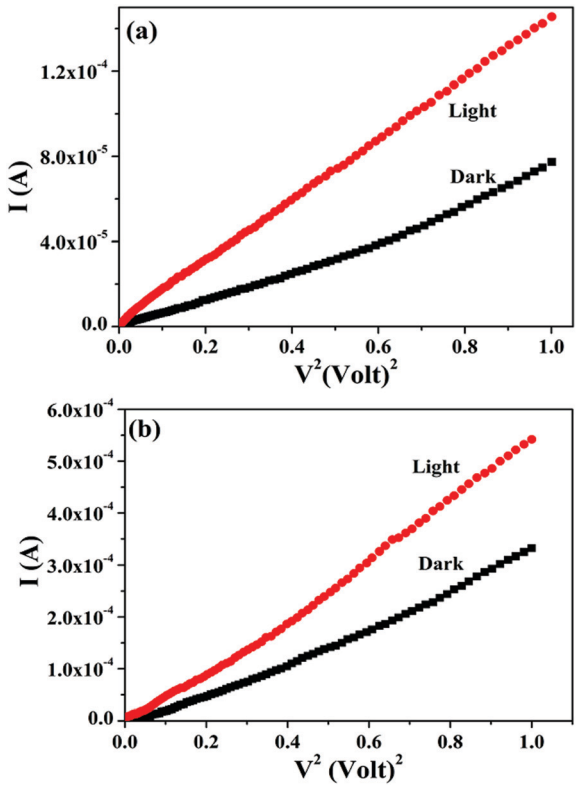


Fig. 15 *I vs.* $V^2$ plot under dark and illumination conditions for (a) device 1 and (b) device 2.

diffusion length ($L_D$), and transit time ($\tau$) *etc.* are calculated using the following set of equations.

$$N = \sigma/(q \cdot \mu_{eff}) \quad (10)$$

$$\tau = (9\varepsilon_0\varepsilon_r V)/(8d \cdot l) \quad (11)$$

$$\mu_{eff} = (q \cdot D)/(k \cdot T) \quad (12)$$

$$L_D = \sqrt{(2D\tau)} \quad (13)$$

The better performance of the SBD device can be categorised by the high values of $N$, $\mu_{eff}$ and $L_D$. All device parameters for both devices are listed in Table S8 (ESI†) (complex **1**) and Table S9 (ESI†) (complex **2**). From the detailed analysis with respect to device performance, it can be concluded that device 2 made from compound **2** is better than device 1. A comparison of the conductivities of the recently reported Ni(II) based complexes with our synthesized complexes **1** and **2** (Table S10, ESI†) shows that our materials have enough potentiality in optoelectronic applications.

## Conclusions

Two new octahedral complexes of nickel(II) have been synthesized and characterized, where both the triazine moiety and pyridine-2,6-dicarboxylic acid act as ligands for complex **1** and only the triazine moiety binds Ni(II) in complex **2**. In the synthesized metal–ligand frameworks, various supramolecular interactions especially π···π stacking, anion···π interactions along with lone pair···π, C–H···π, anion···$\pi^+$, π···$\pi^+$, $\pi^+$···$\pi^+$ and H-bonding interactions are present. These imperative interactions are responsible for the construction of extended networks in the solid state architectures of complexes **1** and **2**. DFT calculations evidence the existence of cooperativity effects in the formation of supramolecular π···π/π···π/π···π interactions for complex **1**. Various anion···π interactions in complex **2** have been well established by using the NCI plot index.

The realistic applications of both the complexes have been initiated by fabricating the SBD device using silver as the metal contact. The devices made from complexes **1** and **2** exhibit non-linear rectifying behaviour under dark and light illumination at an applied potential of ±1.0 V. The measured device parameters, *e.g.*, mobility, transit time, carrier diffusion length, and ideality factor, confirm complex **2** as better SBD compared to complex **1**. A likely explanation for this behaviour can be related to the presence of extensive π···π stacking and a large number of counter-ions in complex **2**. This issue is currently under investigation in our laboratory. Conductivity measurements of the devices further indicated the enhanced charge transportation properties of device 2 compared to that of device 1 under illumination conditions. In fact, both Ni(II) coordination compounds reported herein illustrate reasonably higher electrical conductivities than other Ni-based compounds reported in the literature.

## Conflicts of interest

There are no conflicts to declare.

## Acknowledgements

S. Pramanik acknowledges the Council of Scientific and Industrial Research (CSIR, File no. 09/096(0947)/2018-EMR-I), New Delhi, for the Senior Research Fellowship. The authors acknowledge the MCIU of Spain (project CTQ2017-85821-R, AEI/FEDER, UE funds) for the financial support. S. Jana is grateful to UGC (New Delhi) for DSK Post Doctoral Fellowship, award No.F.4-2/2006(BSR)/CH/18-19/0017.

## References

1 (*a*) M. Du, C.-P. Li, C.-S. Liu and S.-M. Fang, *Coord. Chem. Rev.*, 2013, **257**, 1282–1305; (*b*) K. B. Thapa, Y.-F. Hsu, H.-C. Lin and J.-D. Chen, *CrystEngComm*, 2015, **17**, 7574–7582; (*c*) S. Konar, *Inorg. Chem. Commun.*, 2014, **49**, 76–78; (*d*) S. Konar, A. Dey, S. R. Choudhury, K. Das, S. Chatterjee, P. P. Ray, J. Ortega-Castro, A. Frontera and S. Mukhopadhyay, *J. Phys. Chem. C*, 2018, **122**, 8724–8734.

2 (*a*) L.-P. Xue, Z.-H. Li, L.-F. Ma and L.-Y. Wang, *CrystEngComm*, 2015, **17**, 6441–6449; (*b*) S. Radi, M. El-Massaoudi, H. Benaissa, N. N. Adarsh, M. Ferbinteanu, E. Devlin, Y. Sanakis and Y. Garcia, *New J. Chem.*, 2017, **41**, 8232–8241; (*c*) J. Z. Gu, Y. Cai, X. X. Liang, J. Wu, Z. F. Shi and A. M. Kirillov,

*CrystEngComm*, 2018, **20**, 906–916; (*d*) S. Jia, Z. Gao, N. Tian, Z. Li, J. Gong, J. Wang and S. Rohani, *Chem. Eng. Res. Des.*, 2021, **166**, 268–280.

3 (*a*) B. Gole, A. K. Bar, A. Mallick, R. Banerjee and P. S. Mukherjee, *Chem. Commun.*, 2013, **49**, 7439–7441; (*b*) X.-Q. Guo, C. Huang, H.-Y. Yang, Z.-C. Shao, K. Gao, N. Qin, G.-X. Li, J. Wu and H.-W. Hou, *Dalton Trans.*, 2018, **47**, 16895–16901; (*c*) J. Z. Gu, M. Wen, Y. Cai, Z. F. Shi, A. S. Arol, M. V. Kirillova and A. M. Kirillov, *Inorg. Chem.*, 2019, **58**, 2403–2412.

4 K. J. Lee, J. H. Lee, S. Jeoung and H. R. Moon, *Acc. Chem. Res.*, 2017, **50**, 2684–2692.

5 (*a*) A. C. Kizzie, A. G. Wong-Foy and A. J. Matzger, *Langmuir*, 2011, **27**, 6368–6373; (*b*) K. S. Song, D. Kim, K. Polychronopoulou and A. Coskun, *ACS Appl. Mater. Interfaces*, 2016, **8**, 26860–26867; (*c*) S. Mondal and P. Dastidar, *Cryst. Growth Des.*, 2019, **19**, 470–478.

6 K. Biradha, A. Goswami and R. Moi, *Chem. Commun.*, 2020, **56**, 10824–10842.

7 (*a*) B. Dutta, R. Jana, A. K. Bhanja, P. P. Ray, C. Sinha and M. H. Mir, *Inorg. Chem.*, 2019, **58**, 2686–2694; (*b*) P. Ghorai, A. Dey, A. Hazra, B. Dutta, P. Brandao, P. P. Ray, P. Banerjee and A. Saha, *Cryst. Growth Des.*, 2019, **11**, 6431–6447.

8 (*a*) B. Deka, T. Sarkar, S. Banerjee, A. Kumar, S. Mukherjee, S. Deka, K. K. Saikia and A. Hussain, *Dalton Trans.*, 2017, **46**, 396–409; (*b*) Q.-P. Qin, Z.-F. Wang, S.-L. Wang, D.-M. Luo, B.-Q. Zou, P.-F. Yao, M.-X. Tan and H. Liang, *Eur. J. Med. Chem.*, 2019, **170**, 195–202.

9 (*a*) D. Das and K. Biradha, *Cryst. Growth Des.*, 2018, **18**, 3683–3692; (*b*) B. Parmar, K. K. Bisht, Y. Rachuri and E. Suresh, *Inorg. Chem. Front.*, 2020, **7**, 1082–1107; (*c*) J. Zhu, P. Zhu, M. Yan, H. Chen and K. Zhang, *CrystEngComm*, 2021, DOI: 10.1039/D0CE01724H.

10 (*a*) G. Xu, P. Nie, H. Dou, B. Ding, L. Li and X. Zhang, *Mater. Today*, 2017, **20**, 191–209; (*b*) M. Inukai, S. Horike, T. Itakura, R. Shinozaki, N. Ogiwara, D. Umeyama, S. Nagarkar, Y. Nishiyama, M. Malon, A. Hayashi, T. Ohhara, R. Kiyanagi and S. Kitagawa, *J. Am. Chem. Soc.*, 2016, **138**, 8505–8511.

11 (*a*) M. Guergueb, S. Nasri, J. Brahmi, F. Loiseau, F. Molton, T. Roisnel, V. Guerineau, I. Turowska-Tyrk, K. Aouadi and H. Nasri, *RSC Adv.*, 2020, **10**, 6900–6918; (*b*) M. Dai, H. X. Li and J. P. Lang, *CrystEngComm*, 2015, **17**, 4741–4753; (*c*) J. Huo, D. Yu, H. Li, B. Luo and N. Arulsamy, *RSC Adv.*, 2019, **9**, 39323–39331; (*d*) J. Liu, D. Xie, W. Shi and P. Cheng, *Chem. Soc. Rev.*, 2020, **49**, 1624–1642; (*e*) J. B. Gilroy and E. Otten, *Chem. Soc. Rev.*, 2020, **49**, 85–113.

12 (*a*) N. Li, R. Feng, J. Zhu, Z. Chang and X.-H. Bu, *Coord. Chem. Rev.*, 2018, **375**, 558–586; (*b*) X. Q. Liang, R. K. Gupta, Y. W. Li, H. Y. Ma, L. N. Gao, C. H. Tung and D. Sun, *Inorg. Chem.*, 2020, **59**, 2680–2688.

13 (*a*) J. Kim, B. L. Chen, T. M. Reineke, H. L. Li, M. Eddaoudi, D. B. Moler, M. O'Keeffe and O. M. Yaghi, *J. Am. Chem. Soc.*, 2001, **123**, 8239–8247; (*b*) Y. N. Gong, C. B. Liu, H. L. Wen, L. S. Yan, Z. Q. Xiong and L. Ding, *New J. Chem.*, 2011, **35**, 865–875; (*c*) G. Mahmoudi, F. A. Afkhami, E. Zangrando, W. Kaminsky, A. Frontera and D. A. Safin, *J. Mol. Struct.*, 2021, **1224**, 129188.

14 (*a*) A. Nijamudheen, D. Jose, A. Shine and A. Datta, *J. Phys. Chem. Lett.*, 2012, **3**, 1493–1496; (*b*) O. Perraud, V. Robert, H. Gornitzka, A. Martinez and J.-P. Dutasta, *Angew. Chem., Int. Ed.*, 2012, **51**, 504–508; (*c*) M. K. Bhattacharyya, D. Dutta, S. M. N. Islam, A. Frontera, P. Sharma, A. K. Verma and A. Das, *Inorg. Chim. Acta*, 2020, **501**, 119233.

15 (*a*) M. Mitra, P. Manna, A. Bauzá, P. Ballester, S. K. Seth, S. R. Choudhury, A. Frontera and S. Mukhopadhyay, *J. Phys. Chem. B*, 2014, **118**, 14713–14726; (*b*) A. Das, S. R. Choudhury, B. Dey, S. K. Yalamanchili, M. Helliwell, P. Gamez, S. Mukhopadhyay, C. Estarellas and A. Frontera, *J. Phys. Chem. B*, 2010, **114**, 4998–5009; (*c*) A. Das, S. R. Choudhury, C. Estarellas, B. Dey, A. Frontera, J. Hemming, M. Helliwell, P. Gamez and S. Mukhopadhyay, *CrystEngComm*, 2011, **13**, 4519–4527; (*d*) L. A. Barrios, G. Aromi, A. Frontera, D. Quiñonero, P. M. Deya, P. Gamez, O. Roubeau, E. J. Shotton and S. J. Teat, *Inorg. Chem.*, 2008, **47**, 5873–5881; (*e*) C. Garau, D. Quiñonero, A. Frontera, P. Ballester, A. Costa and P. M. Deyà, *Org. Lett.*, 2003, **5**, 2227–2229; (*f*) A. Bauzá, T. J. Mooibroek and A. Frontera, *CrystEngComm*, 2016, **18**, 10–23.

16 (*a*) P. Manna, S. K. Seth, M. Mitra, A. Das, N. J. Singh, S. R. Choudhury, T. Kar and S. Mukhopadhyay, *CrystEngComm*, 2013, **15**, 7879–7886; (*b*) S. Pramanik, S. Konar, K. Chakraborty, T. Pal, S. Das, S. Chatterjee, M. Dolai and S. Pathak, *J. Mol. Struct.*, 2020, **1206**, 127663.

17 (*a*) J. J. Liu, S. B. Xia, Y. L. Duan, T. Liu, F. X. Cheng and C. K. Sun, *Polymer*, 2018, **10**, 165–176; (*b*) P. Thuéry and J. Harrowfield, *CrystEngComm*, 2015, **17**, 4006–4018; (*c*) Y. Rachuri, B. Parmar, K. K. Bisht and E. Suresh, *Dalton Trans.*, 2017, **46**, 3623–3630.

18 (*a*) S. E. Domínguez, F. E. M. Vieyra and F. Fagalde, *Dalton Trans.*, 2020, **49**, 12742–12755; (*b*) Z. Azarkamanzad, F. Farzaneh, M. Maghami and J. Simpson, *New J. Chem.*, 2019, **43**, 12020–12031; (*c*) A. H. Sun, Q. Wei, A. P. Fu, S. D. Han, J. H. Li and G. M. Wang, *Dalton Trans.*, 2018, **47**, 6965–6972.

19 (*a*) K. Abdi, H. Hadadzadeh, M. Salimi, J. Simpson and A. D. Khalaji, *Polyhedron*, 2012, **44**, 101–112; (*b*) D. A. Safin, J. M. Frost and M. Murugesu, *Dalton Trans.*, 2015, **44**, 20287–20294; (*c*) M. Maghami, F. Farzaneh, J. Simpson, M. Ghiasi and M. Azarkish, *J. Mol. Struct.*, 2015, **1093**, 24–32.

20 (*a*) D. K. Maity, S. Ghosh, K. Otake, H. Kitagawa and D. Ghoshal, *Inorg. Chem.*, 2019, **58**, 12943–12953; (*b*) S. Bala, A. De, A. Adhikary, S. Saha, S. Akhtar, K. S. Das, M.-L. Tong and R. Mondal, *Cryst. Growth Des.*, 2020, **20**, 5698–5708.

21 (*a*) C. W. Machan, M. Adelhardt, A. A. Sarjeant, C. L. Stern, J. Sutter, K. Meyer and C. A. Mirkin, *J. Am. Chem. Soc.*, 2012, **134**, 16921–16924; (*b*) I. Kumar, P. Bhattacharya and K. H. Whitmire, *Organometallics*, 2014, **33**, 2906–2909; (*c*) K. Ghosh, A. Banerjee, A. Bauzá, A. Frontera and S. Chattopadhyay, *RSC Adv.*, 2018, **8**, 28216–28237; (*d*) Q.-P. Qin, Z.-F. Wang, M.-X. Tan, X.-L. Huang, H.-H. Zou, B.-Q. Zou, B.-B. Shi and S.-H. Zhang, *Metallomics*, 2019, **11**, 1005–1015; (*e*) M. D. Olawale, J. O. Obaleyeb and E. O. Oladelec, *New J. Chem.*, 2020, **44**, 18780–18791.

22 (*a*) K. Sinziger, S. Hünig, M. Jopp, D. Bauer, W. Bietsch, J. U. von Schütz, H. C. Wolf, R. K. Kremer, T. Metzenthin,

 

R. Bau, S. I. Khan, A. Lindbaum, C. L. Lengauer and E. Tillmans, *J. Am. Chem. Soc.*, 1993, **115**, 7696–7705; (*b*) R. Kato, H. Kobayashi, A. Kobayashi, T. Mori and H. Inokuchi, *Chem. Lett.*, 1987, 1579–1582; (*c*) R. Kato, H. Kobayashi and A. Kobayashi, *J. Am. Chem. Soc.*, 1989, **111**, 5224–5232.

23 (*a*) S. Hünig and P. Erk, *Adv. Mater.*, 1991, **3**, 225–236; (*b*) D. Asakura, C. H. Li, Y. Mizuno, M. Okubo, H. Zhou and D. R. Talham, *J. Am. Chem. Soc.*, 2013, **135**, 2793–2799.

24 (*a*) L. Welte, A. Calzolari, R. di Felice, F. Zamora and J. Gómez-Herrero, *Nat. Nanotechnol.*, 2010, **5**, 110–115; (*b*) W. Shi, G. Wu, X. Yong, T. Deng, J. S. Wang, J. C. Zheng, J. Xu, M. B. Sullivan and S. W. Yang, *ACS Appl. Mater. Interfaces*, 2018, **10**, 35306–35315; (*c*) V. Rubio-Giménez, S. Tatay and C. Martí-Gastaldo, *Chem. Soc. Rev.*, 2020, **49**, 5601–5638.

25 C. Adamo and V. Barone, *J. Chem. Phys.*, 1999, **110**, 6158–6170.

26 S. Grimme, J. Antony, S. Ehrlich and H. Krieg, *J. Chem. Phys.*, 2010, **132**, 154104.

27 F. Weigend, *Phys. Chem. Chem. Phys.*, 2006, **8**, 1057–1065.

28 M. J. Frisch, G. W. Trucks, H. B. Schlegel, G. E. Scuseria, M. A. Robb, J. R. Cheeseman, G. Scalmani, V. Barone, B. Mennucci, G. A. Petersson, H. Nakatsuj, M. Caricato, X. Li, H. P. Hratchian, A. F. Iamaylov, J. Bloino, G. Zheng, J. L. Sonnenberg, M. Hada, M. Ehara, K. Toyota, R. Fukuda, J. Hasegawa, M. Ishida, T. Nakajima, Y. Honda, O. Kitao, H. Nakai, T. Vreven, J. A. Montgomery Jr, J. E. Peralta, F. Ogliaro, M. Bearpark, J. J. Heyd, E. Brothers, K. N. Kudin, V. N. Staroverov, R. Kobayashi, J. Normand, K. Raghavachari, A. Rendell, J. C. Burant, S. S. Lyengar, J. Tomasi, M. Cossi, N. Rega, J. M. Millam, M. Klene, J. E. Knox, J. B. Cross, V. Bakken, C. Adamo, J. Jaramillo, R. Gomperts, R. E. Stratmann, O. Yazyev, A. J. Austin, R. Cammi, C. Pomelli, J. W. Ochterski, R. L. Martin, K. Morokuma, V. G. Zakrzewski, G. A. Voth, P. Salvador, J. J. Dannenberg, S. Dapprich, A. D. Daniels, O. Farkas, J. B. Foresman, J. V. Ortiz, J. Cioslowski and D. J. Fox, *Gaussian 09, Revision A.1*, Gaussian Inc., Wallingford CT, 2016.

29 R. F. W. Bader, *Chem. Rev.*, 1991, **91**, 893–928.

30 E. R. Johnson, S. Keinan, P. Mori-Sánchez, J. Contreras-García, A. J. Cohen and W. Yang, *J. Am. Chem. Soc.*, 2010, **132**, 6498–6506.

31 J. Contreras-García, E. R. Johnson, S. Keinan, R. Chaudret, J.-P. Piquemal, D. N. Beratan and W. Yang, *J. Chem. Theory Comput.*, 2011, **7**, 625–632.

32 T. A. Keith, AIMALL (Version 19.02.13), TK Gristmill Software, Overl. Park KS, USA, 2019.

33 L. E. Zelenkov, D. M. Ivanov, K. Sadykov, N. A. Bokach, B. Galmes, A. Frontera, V. Yu. Kukushkin and Yu. Vadim, *Cryst. Growth Des.*, 2020, **20**, 6956–6965.

34 Bruker, SMART $\nu$5.631, Bruker AXS Inc., Madison, WI, USA,2001.

35 G. M. Sheldrick, *SHELXL-2014/7: Program for the Solution of Crystal Structures*, University of Gottingen, Gottingen, Germany, 2014.

36 P. Manna, S. K. Seth, M. Mitra, S. R. Choudhury, A. Bauzá, A. Frontera and S. Mukhopadhyay, *Cryst. Growth Des.*, 2014, **14**, 5812–5821.

37 S. M. Sze, *Physics of Semiconductor Devices*, Wiley, New York, 1969, p. 496.

38 J. G. Simmons, *Phys. Rev.*, 1967, **155**, 657–660.

39 S. K. Cheung and N. W. Cheung, *Appl. Phys. Lett.*, 1986, **49**, 85–87.

40 M. W. Allen and S. M. Durbin, *Appl. Phys. Lett.*, 2008, **92**, 12110–12113.

41 D. T. Quan and H. Hbib, *Solid-State Electron.*, 1993, **36**, 339–344.

42 A. Jain, P. Kumar, S. C. Jain, V. Kumar, R. Kaur and R. M. Mehra, *J. Appl. Phys.*, 2007, **102**, 094505.

43 S. Aydogan, M. Saglam and A. Turut, *J. Phys.: Condens. Matter*, 2006, **18**, 2665–2676.

44 Z. Ahmad and M. H. Sayyad, *Phys. E*, 2009, **41**, 631–634.

45 P. Kumar, S. C. Jain, V. Kumar, S. Chand and R. P. Tandon, *J. Appl. Phys.*, 2009, **105**, 104507.

46 S. Suresh, *Int. J. Phys. Sci.*, 2013, **8**, 1121–1127.

47 P. W. M. Blom, M. J. M. D. Jong and M. G. V. Munster, *Phys. Rev. B: Condens. Matter Mater. Phys.*, 1997, **55**, 656–659.